Available online at www.sciencedirect.com

SCIENCE DIRECT®

International Journal of Heat and Mass Transfer 47 (2004) 257–269

International Journal of HEAT and MASS TRANSFER

www.elsevier.com/locate/ijhmt

Three-dimensional numerical simulation of convection and radiation in a differentially heated cavity using the discrete ordinates method

G. Colomer [*], M. Costa, R. Cònsul, A. Oliva

Centre Tecnològic de Transferència de Calor, Lab. Termotècnia i Energètica, Universitat Politècnica de Catalunya (UPC), ETSEIT, C/Colom 11, 08222 Terrassa, Spain

Received 18 December 2002; received in revised form 11 July 2003

Abstract

The main purpose of this paper is to study, in a three-dimensional, differentially heated cavity, the phenomenon of radiation and natural convection in both transparent and participating media. The discrete ordinates method (DOM) is used to solve the radiative transfer equation. The Navier–Stokes equations (NSE), describing natural convection, are solved with a segregated SIMPLE-like algorithm. For non-participating media, the coupling between the radiative transfer and NSE is done via the radiative heat exchange between surfaces. For participating media, a source term is added in the energy equation. The local and mean heat flux as a function of the Rayleigh number is studied, for both transparent and participating media with different optical thicknesses. The effect of the Planck number on the heat flux is also analyzed for different values of the Rayleigh number. Also, a comparison between a purely two-dimensional case and the results obtained in the mid-plane of a long rectangular enclosure is presented.

Keywords: Radiation; Three-dimensional; Discrete ordinates method (DOM); Natural convection; Participating media

1. Introduction

Research on the analysis and numerical resolution of heat transfer and fluid flow phenomena where radiant heat exchange has an essential contribution, becomes a key aspect for the employment of CFD simulations as a worthwhile complement to experimental research into industry-related problems. These problems involve the resolution of the Navier–Stokes equations (NSE) and the radiative transfer equation (RTE). The resolution of the RTE implies a considerable computational cost due to the directional nature of the intensity radiation field. This high computational cost limits detail in the simulation of coupled radiation and convection. Therefore, improvements of the numerical methods and fundamental analysis of this complex phenomena have motivated interest in the scientific community.

The main purpose of this paper is the analysis of natural convection phenomenon coupled with radiant exchange in a three-dimensional differentially heated cavity. The differential heated cavity problem is a classical benchmark test commonly used in the process of CFD codes verification. In this sense, numerical results presented in this work are also addressed to the CFD developers in the task of verifying their codes. Although benchmark solutions can be found for both 2D and 3D discretizations, as in [1–5], the consideration of radiation effects is restricted to 2D geometries. There are also reported solutions to three-dimensional problems [6,7], but only taking into account the radiative heat transfer.

The proposed problem has been solved for a range of Rayleigh and Planck numbers, which are the relevant dimensionless numbers for this case, and considering both transparent and gray, purely absorbing

---

[*] Corresponding author. Tel.: +34-93-739-8192.
E-mail address: labtie@labtie.mmt.upc.es (G. Colomer).

0017-9310/$ - see front matter © 2003 Elsevier Ltd. All rights reserved.
doi:10.1016/S0017-9310(03)00387-9

Nomenclature

c_p	specific heat [J K^{-1} kg^{-1}]
$\vec{g}$	gravitational field [m s^{-2}], $\vec{g} = g\hat{u}_g$
I^*	dimensionless intensity radiation field, $I/\sigma_B T_c^4$
I_B	blackbody emission [W m^{-2}]
k	thermal conductivity [W m^{-1} K^{-1}]
L	length of cubic cavity [m]
N_a, N_p	number of azimuthal and polar directions
P^*	dimensionless pressure, $P/(L\rho_0 g\beta\Delta T)$
Pl	Planck number, $k\Delta T/(L\sigma_B T_c^4)$
Pr	Prandtl number, $\mu c_p/k$
Q^*	dimensionless total heat flux, $Q_c^* + Q_r^*$
Q_c^*	dimensionless convective heat flux, $-(L\partial T/\partial x)/\Delta T$
Q_r^*	dimensionless radiative heat flux, $LQ_r/k\Delta T$
Ra	Rayleigh number, $g\beta\Delta T L^3 \rho_0^2 c_p/(k\mu)$
$\hat{s}_i$	discrete ordinate
T^*	dimensionless temperature, $(T - T_c)/\Delta T$

T_0	mean temperature, $(T_h + T_c)/2$ [K]
T_0^*	reference temperature ratio, $T_c/\Delta T$
T_c, T_h	cold and hot temperatures [K]
ΔT	temperature gap, $T_h - T_c$ [K]
$\vec{v}^*$	dimensionless velocity, $\vec{v}/\sqrt{Lg\beta\Delta T}$
x^*, y^*, z^*	dimensionless coordinates, x/L, y/L, z/L
Greek symbols	
β	thermal expansion coefficient [K^{-1}]
δ	difference between two meshes
κ	absorption coefficient [m^{-1}]
μ	dynamic viscosity [kg m^{-1} s^{-1}]
μ_i, ν_i	direction cosines
ρ_0	reference density [kg m^{-3}]
σ_B	Stephan–Boltzmann constant
τ	optical thickness, κL
Symbol	
$\vec{\nabla}^*$	dimensionless derivative, $L\vec{\nabla}$

homogeneous medium. In the latter case different optical thickness are considered. The effects of radiation are shown and compared to the case where radiation is neglected. The radiation contribution is solved using the discrete ordinates method (DOM), first developed in radiative transfer problems by Truelove [8] and Fiveland [9]. Special emphasis is given to its special features when solving three-dimensional problems.

2. Discretization of the RTE using the discrete ordinates method

The RTE, used to determine the intensity radiation field, accounts for the variation of the energy carried by a ray beam in direction $\hat{s}$ due to its interaction with the medium in which it is propagating. The equation that properly describes such variation, for a gray and purely absorbing (non-scattering) medium with absorption coefficient κ, reduces to

$$\hat{s} \cdot \vec{\nabla} I(\vec{r}, \hat{s}) = -\kappa(I(\vec{r}, \hat{s}) - I_B(\vec{r})) \qquad (1)$$

which is a conservation optical balance equation. Once the intensity radiation field is known, the energy flux due to radiation through an arbitrarily oriented surface, whose perpendicular vector is $\hat{n}$, can be calculated as:

$$Q_r(\hat{n}) = \int_{4\pi} (\hat{n} \cdot \hat{s}) I(\vec{r}, \hat{s})\, d\hat{s} \qquad (2)$$

The outstanding aspect of DOM is that such an integral is computed with a low computational cost method, which is analogous to the Gauss–Legendre method. It consists of the substitution of the integral with a weighted summation of the integrand at selected points (ordinates) of the integration domain. The following assumption is made:

$$\int_{4\pi} (\hat{n} \cdot \hat{s}) I(\vec{r}, \hat{s})\, d\hat{s} \simeq \sum_{i=1}^{N} \omega_i (\hat{n} \cdot \hat{s}_i) I^i \qquad (3)$$

The choice of the weights and ordinates must be done carefully, and there are several ways to proceed [9–11]. In the following section, a method to choose the ordinates, which is suitable for three-dimensional geometries, is presented. Once the N ordinates are chosen, the differential equation (1) is solved precisely for such directions and becomes a linear system of N differential equations. The resulting linear system can be written as

$$\hat{s}_i \cdot \vec{\nabla} I^i = -\kappa I^i + \kappa I_B \qquad (4)$$

for $1 \leqslant i \leqslant N$. $\hat{s}_i$ stands for the ith discretized ordinate. The right hand side of Eq. (4) accounts for the effects exerted by the medium on the intensity radiation field.

The discretization of the variation term, that is, the left hand side of Eq. (1), is straightforward in cartesian coordinates. In Fig. 1(a), the precise definition of the $\hat{s}_i$ direction is shown. To simplify the notation, the shortcuts $\mu_i = \cos\theta_i$ and $\nu_i = \cos\varphi_i$ are defined. Also, μ_i^* is defined as $\mu_i^* = (1 - \mu_i^2)^{1/2}$ (resp. ν_i^*). It is therefore not difficult to see that

$$\hat{s}_i \cdot \vec{\nabla} I^i = \mu_i \nu_i \frac{\partial I^i}{\partial x} + \mu_i^* \frac{\partial I^i}{\partial y} + \mu_i \nu_i^* \frac{\partial I^i}{\partial z}$$

Next, the finite volume technique is applied, which consists of the integration of the RTE equation over a

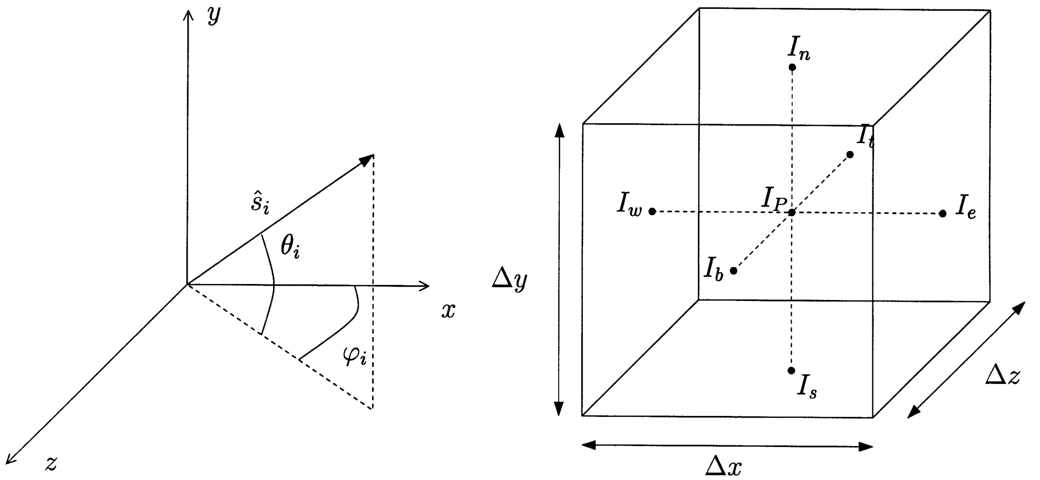

(a) (b)

Fig. 1. Discretization of the RTE. Definition of direction $\hat{s}_i$ (a) and typical control volume (b).

control volume such as that shown in Fig. 1(b). The result is an equation relating the value of the intensity at the nodal point, I_P^i, to the intensity at each adjacent face I_e^i, I_w^i, I_n^i, I_s^i, I_t^i and I_b^i. By assuming a linear relation such as $I_P^i = fI_\mathrm{e}^i + (1-f)I_\mathrm{w}^i$ (and the same for the y- and z-axis) the intensity radiation field at P can be explicitly written in terms of the values of the intensity field on three faces. The factor f accounts for different numerical schemes in a single formulation.

For each control volume, the explicit value of intensity at nodal point P is

$$I_P^i = \frac{\mu_i \nu_i \Delta y \Delta z I_x^i + \mu_i^* \Delta x \Delta z I_y^i + \mu_i \nu_i^* \Delta x \Delta y I_z^i + f\kappa I_\mathrm{B} \Delta x \Delta y \Delta z}{\mu_i \nu_i \Delta y \Delta z + \mu_i^* \Delta x \Delta z + \mu_i \nu_i^* \Delta x \Delta y + f\kappa \Delta x \Delta y \Delta z} \qquad (5)$$

where, for instance, I_x^i equals I_w^i for radiation travelling from west to east, i.e. $-\pi/2 \leqslant \varphi_i \leqslant \pi/2$ and I_x^i equals I_e^i otherwise —see Fig. 1(a). Similar considerations apply for I_y^i and I_z^i. All the results given throughout the paper were obtained with an upwind scheme, that is, by setting $f = 1$.

It is important to recall that, strictly speaking, the above discretization is valid for a given wavelength. While we consider gray media here, the method can be easily extended to non-gray media.

3. Choosing the discrete ordinates

The proper choice of weights and ordinates is very important, even in the simplest of cases where weights are taken to be constant. All results presented here make use of such a constant weight scheme.

One special requirement when choosing the discrete ordinates is the conservation of energy, that is, discrete ordinates and weights must give an exact value of the integral in Eq. (2). Whatever the set of ordinates chosen, it must satisfy the discretized equivalent condition which, according to Fig. 1(a), can be written as

$$\sum_i \mu_i \nu_i = \sum_i \mu_i^* = \sum_i \mu_i \nu_i^*. \qquad (6)$$

The condition of energy conservation that should satisfy $\hat{s}_i$ comes from Eq. (3) with $\hat{n} \in \{\hat{\imath}, \hat{\jmath}, \hat{k}\}$ and $\hat{n} \cdot \hat{s} \geqslant 0$. In order to find the correct weight, it should be noted that, for example, the evaluation of Eq. (3) for $\hat{n}$ parallel to the x-axis and constant intensity radiation field is

$$\pi = \int_{\hat{\imath}\cdot\hat{s} \geqslant 0} (\hat{\imath} \cdot \hat{s})\, \mathrm{d}\hat{s} \simeq 4\omega \sum_i \mu_i \nu_i, \qquad (7)$$

where an additional factor of 4 appears since the ordinates are only defined for one octant and the sum extends over four octants. A set of directions verifying the above conditions can be obtained as follows: given N_p and N_a directions with constant polar (resp. azimuthal) angle θ_l (resp. φ_m), N is the total number of ordinates in an octant $N = N_\mathrm{a} N_\mathrm{p}$. Therefore the values of the angles are

$$\varphi_m = \frac{\pi}{4N_\mathrm{a}}(2m-1) \quad \text{and} \quad \theta_l = \alpha + (l-1)\gamma,$$

where $1 \leqslant m \leqslant N_\mathrm{a}$ and $1 \leqslant l \leqslant N_\mathrm{p}$. Also $\alpha = \arctan\xi - \pi(N_\mathrm{p}-1)/6N_\mathrm{p}$, $1/\xi = 2N_\mathrm{a}\sin(\pi/4N_\mathrm{a})$ and $\gamma = \pi/3N_\mathrm{p}$.

With those definitions of the discretized directions, it can be seen, by taking the limits $N_\mathrm{p} \to \infty$ and $N_\mathrm{a} \to \infty$, that while the azimuthal angles φ_m lie in the range between 0 and $\pi/2$, the polar angles θ_l lie in a narrower range, approximately $\pi/6$ radians above and below an angle of $\arctan(2/\pi)$ ($\simeq 32.5°$), thus not covering the whole octant. Despite this limitation, when the results

Table 1
Directions and weights in the first octant ($x \geqslant 0$, $y \geqslant 0$ and $z \geqslant 0$) used to solve the RTE, all angles are in radians

Direction	θ_i	φ_i	Weight
$\hat{s}_1$	0.229613	0.392699	0.261799
$\hat{s}_2$	0.229613	1.178097	0.261799
$\hat{s}_3$	0.578679	0.392699	0.261799
$\hat{s}_4$	0.578679	1.178097	0.261799
$\hat{s}_5$	0.927745	0.392699	0.261799
$\hat{s}_6$	0.927745	1.178097	0.261799

obtained with this set of ordinates are compared to the results obtained with more general sets, such as those in [10] (p. 546, the so-called S_8 approximation), there is a good agreement. The comparison was made for radiative equilibrium as well as for combined conduction and radiation cases.

A number of ordinates must be chosen taking into account that accurate results with admissible computational cost are desired. Three-dimensional DOM calculations for rectangular furnaces (such as the one in [6]) give accurate results with three directions per octant. Assuming that this accuracy will also hold for the differentially heated cavity, the choice $N_p = 3$ and $N_a = 2$ seems to be a reliable one. The resulting weights and ordinates are given in Table 1.

4. The coupling between radiation and convection

The flow is assumed to be laminar and steady state. All physical properties are taken to be constant, except for the density to allow natural convection. The usual Boussinesq approximation is used for the density in the body force term

$$\rho = \rho_0(1 - \beta(T - T_0))$$

Under these assumptions, the NSE together with the energy equation can be written in dimensionless form as follows:

$$\vec{\nabla}^* \cdot \vec{v}^* = 0 \qquad (8)$$

$$(\vec{v}^* \cdot \vec{\nabla}^*)\vec{v}^* = -\vec{\nabla}^* P^* + \sqrt{\frac{Pr}{Ra}}\nabla^{*^2}\vec{v}^* + \left(T^* - \frac{1}{2}\right)\hat{u}_g \qquad (9)$$

$$\sqrt{RaPr}(\vec{v}^* \cdot \vec{\nabla}^*)T^* = \nabla^{*^2}T^* - \vec{\nabla}^* \cdot \vec{Q}_{\mathrm{r}}^* \qquad (10)$$

where the radiative dimensionless divergence term is calculated as the difference between the emission and the absorption:

$$\vec{\nabla}^* \cdot \vec{Q}_{\mathrm{r}}^* = \frac{\tau}{Pl}\left[4\left(\frac{T^*}{T_0^*} + 1\right)^4 - \int_{4\pi} I^*(\vec{r}, \hat{s})\,\mathrm{d}\hat{s}\right] \qquad (11)$$

and $I^*(\vec{r}, \hat{s})$ is the dimensionless intensity radiation field which solves equation (1).

For the optically thick limit (i.e. $\tau \to \infty$) the additive model was considered. This model consists in independently solving the radiative equilibrium case for a large optical thickness and the NSE without taking into account radiation effects. Therefore, the total heat flux is the addition of the heat flux given by each independent solution.

The flow structure and the temperature distribution are governed, for a given optical thickness τ, by the Rayleigh number (Ra), the Prandtl number (Pr), the Planck number (Pl) and T_0^*,

$$Ra = \frac{g\beta\Delta T L^3 \rho_0^2 c_p}{k\mu}; \quad Pr = \frac{\mu c_p}{k};$$
$$Pl = \frac{k\Delta T}{L\sigma_{\mathrm{B}} T_{\mathrm{c}}^4}; \quad T_0^* = \frac{T_{\mathrm{c}}}{\Delta T} \qquad (12)$$

The Planck number is a measure of the conduction heat transfer relative to a mean heat transfer due to radiation. It is clear from Eqs. (11) and (12) that, as the thermal conductivity k increases, the Planck number also increases and the radiation effects become less noticeable. The adiabatic boundary condition includes a conduction term and a radiation term $Q_{\mathrm{r}}^*(\hat{n})$, calculated with the aid of Eq. (2). The temperature at any of the adiabatic walls is such that

$$\hat{n} \cdot \vec{\nabla}^* T^* = Q_{\mathrm{r}}^*(\hat{n}). \qquad (13)$$

For transparent media, radiation effects depend only on the temperature of the boundaries, since $\vec{\nabla} \cdot \vec{Q}_{\mathrm{r}}^*$ is zero inside the enclosure. From the above boundary condition it is clear that, for a large Planck number, the radiation effects may be discarded since the temperature gradient will be almost zero—the boundary condition required when radiation effects are ignored.

5. Code verification

The numerical code employed in this work was verified by means of the resolution of several benchmark problems, some of them with analytical solutions and others given in the literature. Among them, the code was verified considering problems where radiation plays a dominant role, problems with transparent and participating media and problems considering 2D-coupled radiation and natural convection. The main results of this verification process are described in [5].

In this work, the verification of three-dimensional geometries has been completed and the simulation of a rectangular furnace has been taken into account, comparing the results obtained with those presented by Mengüç and Viskanta [7]. This comparison is described in detail in the next section.

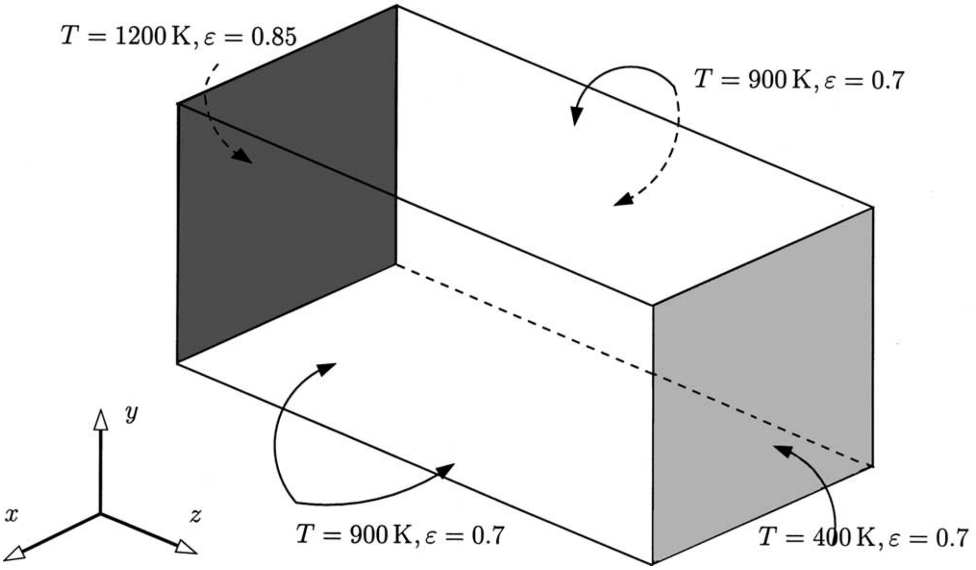

Fig. 2. Problem description of the validation case.

5.1. Rectangular furnace

The three-dimensional rectangular furnace studied encloses a purely absorbing medium (see Fig. 2). The dimensions are 2 m×2 m×4 m—in the x, y and z directions respectively. The walls of the small faces are at 1200 and 400 K while the other four walls are maintained at 900 K. The walls are supposed to reflect and emit diffusively, and to have emissivities of 0.85 for the hot wall and 0.7 for the remaining walls.

In this problem, conduction and convection effects are neglected. Hence, the medium is assumed to be at radiative equilibrium, with an additional homogeneous heat source of $\mathscr{S} = 5$ kW/m^3. The radiative equilibrium condition implies that the only term in the energy equation is the divergence of radiative heat. In the presence of a source term $\mathscr{S}$, the energy equation is simply $\vec{\nabla} \cdot \vec{Q}_{\mathrm{r}} + \mathscr{S} = 0$. Using the dimensional form of Eq. (11), the temperature that makes the energy equation hold can be calculated as

$$T_{\mathrm{re}}(\vec{r}) = \left(\frac{1}{4\sigma_{\mathrm{B}}}\left[\int_{4\pi} I(\vec{r},\hat{s})\,\mathrm{d}\hat{s} - \frac{\mathscr{S}}{\kappa}\right]\right)^{\frac{1}{4}}$$

Two different absorption coefficients, $\kappa = 0.5$ m^{-1} and $\kappa = 1$ m^{-1}, are considered. The results plotted in Figs. 3 and 4 and were computed with a 40×40×80 control volume mesh, considering $N_{\mathrm{p}} = 4$ and $N_{\mathrm{a}} = 3$.

The temperature distribution at mid-height on the hot wall (for $z = 2$ m and $y = 1$ m) is plotted as a function of the dimensionless x^* direction in Fig. 3. The agreement between the results presented in [7] and the results obtained with the DOM method is quite good. It can be observed that temperatures near the walls are not exactly the imposed wall temperatures (900 K); the reason being that heat conduction has been neglected.

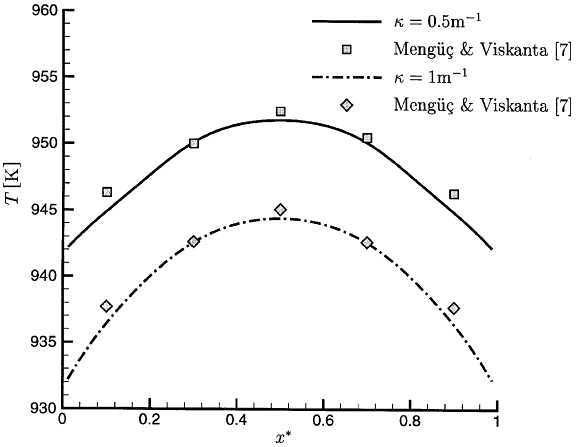

Fig. 3. Temperature profiles for $z = 2$ m. Data from Ref. [7] corresponds to zonal method.

The net heat flux on the hot wall and at mid-height ($z = 0$ m and $y = 1$ m) as a function of the dimensionless x^* direction is plotted in Fig. 4. Lower net heat fluxes in comparison with those reported in [7] are obtained, especially for the optically thinner medium. The differences may be due to the fact that a coarser mesh than the one used in this work was used in [7], and also that the

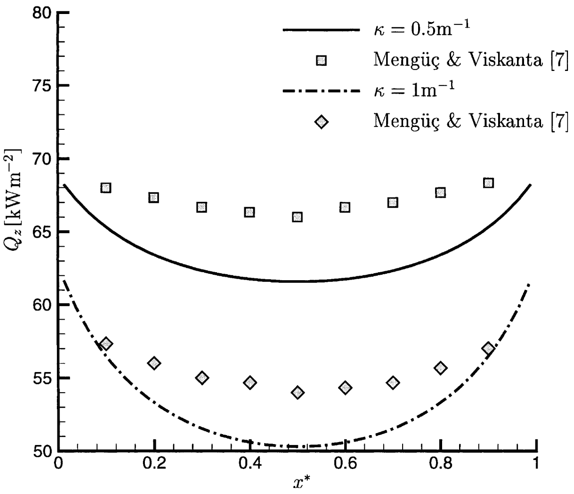

Fig. 4. Radiation heat flux at hot wall. Data from Ref. [7] corresponds to P_3 method.

RTE was solved using spherical harmonics decomposition (P_3 approximation). It has been shown that the differential approximations of the P_3 method are not reliable for optically thin media ($\kappa < 1$) [12]. In addition, it has also been shown that the P_3 method over-predicts the heat flux values in these situations, which is consistent with the results obtained here with the DOM.

6. Numerical results

A cubic enclosure containing a gray fluid is assumed, shown in Fig. 5. Both transparent and participating medium are considered. The west wall is at T_h and the east wall at T_c with $T_h > T_c$. The remaining four walls are adiabatic. The walls of the cavity have been treated as black bodies. The Prandtl number has been fixed to 0.71, and a range of Rayleigh numbers, from $Ra = 10^3$ to 10^6, is studied. In the case of a transparent medium, a longer cavity is also solved, where the depth of the domain is four times that of the cube. The solution of this stretched cavity is compared to a purely two-dimensional differentially heated cavity.

Results are presented for the dimensionless total heat flux at the hot wall, which can be calculated as

$$Q^* = \left(-\frac{\partial T^*}{\partial x^*} + Q_r^* \right)_{x^*=0} \tag{14}$$

Q^* has been considered the significant result to be presented for the three-dimensional differential cavity solutions throughout this paper. Whenever possible, radiation and convection contributions (Q_r^* and Q_c^*) to the total heat transfer are given.

6.1. Discretization

A study was performed to analyze the influence of the mesh spacing on the final result. Four different meshes, with 17^3, 33^3, 65^3 and 97^3 control volumes were used for what was considered to be a reference problem ($Ra = 10^6$, $Pr = 0.71$, $Pl = 0.016$, $T_0^* = 17$ and $\tau = 1$). The conclusions obtained in this single problem have been assumed for the range of governing numbers presented in this paper.

The convergence to an asymptotic solution can be observed by evaluating the mean differences of temperature, radiative heat and velocity fields between one

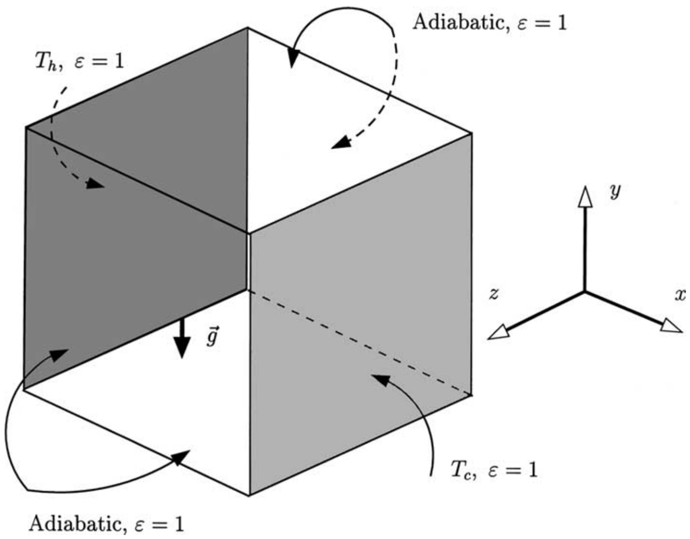

Fig. 5. Three-dimensional differential heated cavity scheme.

Table 2
Mean difference for temperature, radiative heat and velocity fields between two consecutive meshes, and mean heat flux at hot wall for the benchmark differential heated cavity problem

Mesh	$\overline{\delta(T^*)}$	$\overline{\delta(Q^*_{\mathrm{r}})}$	$\overline{\delta(v^*_x)}$	$\overline{\delta(v^*_y)}$	$\overline{\delta(v^*_z)}$	$\overline{Q^*}$
17×17×17	–	–	–	–	–	14.42
33×33×33	2.0%	2.9%	2.7%	2.0%	2.1%	14.28
65×65×65	1.0%	1.5%	1.5%	1.1%	1.3%	13.84
97×97×97	0.2%	0.4%	0.6%	0.4%	0.4%	13.75

$Ra = 10^6$, $Pr = 0.71$, $Pl = 0.016$, $T^*_0 = 17$ and $\tau = 1$.

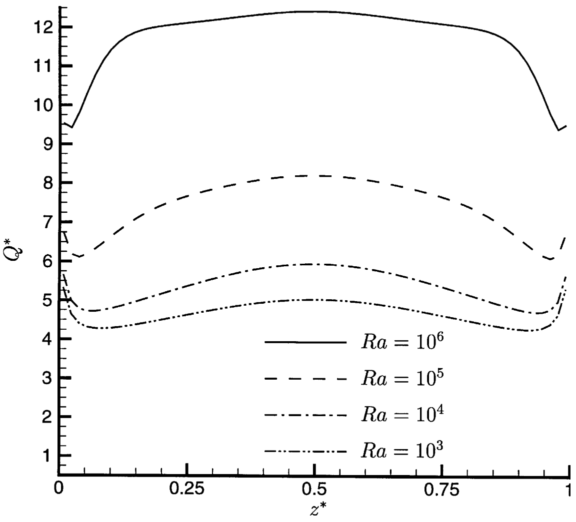

Fig. 6. Average heat flux in the y^* direction versus depth z^*. Transparent medium, $\tau = 0$, $Pl = 0.043$, $T^*_0 = 15$ and $Pr = 0.71$.

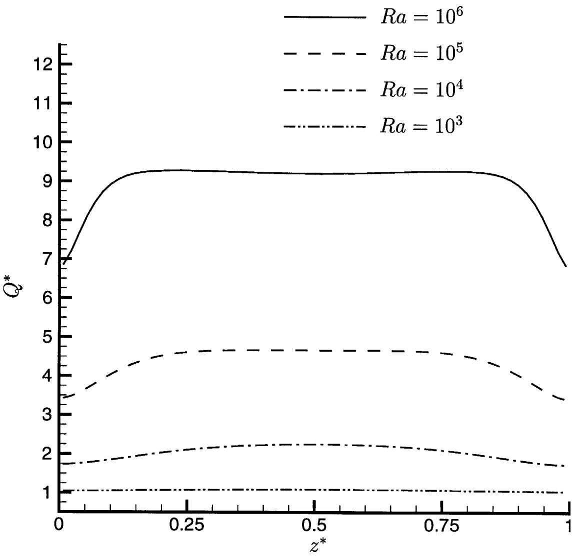

Fig. 7. Average heat flux in the y^* direction versus the depth z^* without radiation. $Pr = 0.71$.

simulation and its previous coarser solution. In Table 2, the mean differences and mean heat flux at the hot wall are shown. As can be seen, differences lower than 1% are obtained comparing the third and fourth discretizations. These results motivate the selection of the third mesh (i.e. the mesh with 65^3 control volumes) as fine enough to perform the numerical studies. The set of ordinates used for this benchmark problem is that obtained with $N_{\mathrm{p}} = 3$ and $N_{\mathrm{a}} = 2$ (Table 1).

Table 3
Hot wall average heat flux

Ra	With radiation			Without radiation	
	Q^*	Q^*_{r}	Q^*_{c}	Q^*	Fusegi and Min Hyun [1]
10^3	4.596	3.162	1.434	1.055	1.085
10^4	5.295	3.233	2.062	2.030	2.100
10^5	7.368	3.385	3.983	4.334	4.361
10^6	11.670	3.568	8.102	8.862	8.770

Q^*_{r} and Q^*_{c} are the radiation and convection contribution to the total heat flux. $Pl = 0.043$, $T^*_0 = 15$, $\tau = 0$ and $Pr = 0.71$.

Table 4
Local extreme values for velocity and heat flux

	$Ra = 10^3$	$Ra = 10^4$	$Ra = 10^5$	$Ra = 10^6$
v^*_x max	0.1250	0.2170	0.1869	0.1284
y^*	0.808	0.838	0.869	0.900
z^*	0.500	0.500	$0.285^{\dagger}$	$0.208^{\dagger}$
v^*_y max	0.1271	0.2333	0.2865	0.2985
x^*	0.177	0.131	0.069	0.038
z^*	0.500	$0.269^{\dagger}$	$0.115^{\dagger}$	$0.069^{\dagger}$
Q^* max	6.350	7.238	10.793	19.168
y^*	∼0	∼0	0.192	0.069
z^*	0.500	0.500	0.500	$0.208^{\dagger}$
Q^* min	3.960	3.729	3.724	4.025
y^*	0.900	0.900	0.931	0.961
z^*	$0.085^{\dagger}$	$0.100^{\dagger}$	$0.085^{\dagger}$	$0.038^{\dagger}$

v^*_x max refers the plane $x^* = 0.5$ and v^*_y max to the plane $y^* = 0.5$. The maximum and minimum heat flux refer to the hot wall ($x^* = 0$). The ∼0 indicates that the maximum was obtained on the first calculation node. The † symbol indicates that the same value was also obtained at location $1 - z^*$. All variables are symmetric respect to the plane $z^* = 0.5$. Transparent medium, $\tau = 0$, $Pl = 0.043$, $T^*_0 = 15$ and $Pr = 0.71$.

6.2. Transparent medium

The medium is assumed to be non-participating ($\tau = 0$). The Planck number is set to $Pl = 0.043$ and $T_0^* = 15$. For the stretched cavity, the number of control volumes is doubled in the z-direction.

The first result presented in Fig. 6 shows the averaged heat flux (in y^* direction) at the hot wall as a function of the position along the z-axis when radiation is taken into account. The simple case when radiation heat exchange is ignored is plotted in Fig. 7. When both figures are compared, it can be seen that radiation significantly increases the heat transfer. The increase of the heat flux is greatest for low Rayleigh numbers. The reason is that the contribution of convection heat transfer becomes more important as Rayleigh number increases, and the contribution of radiative heat transfer remains almost constant (the Planck number has been kept constant). The velocity field only affects the radiation field slightly, through the variation of the temperature at the adiabatic walls, according to Eq. (13).

The effect of radiation and convection on the heat flux can clearly be seen in Table 3, where the average heat flux is given. In Table 4 some local values of the velocity field and heat flux are given. It can also be observed in Fig. 6 that there is an increase of the heat flux at both ends of the z-axis when radiation is present. This effect is more intense for low Rayleigh numbers. This increase is due to the influence of the nearby walls.

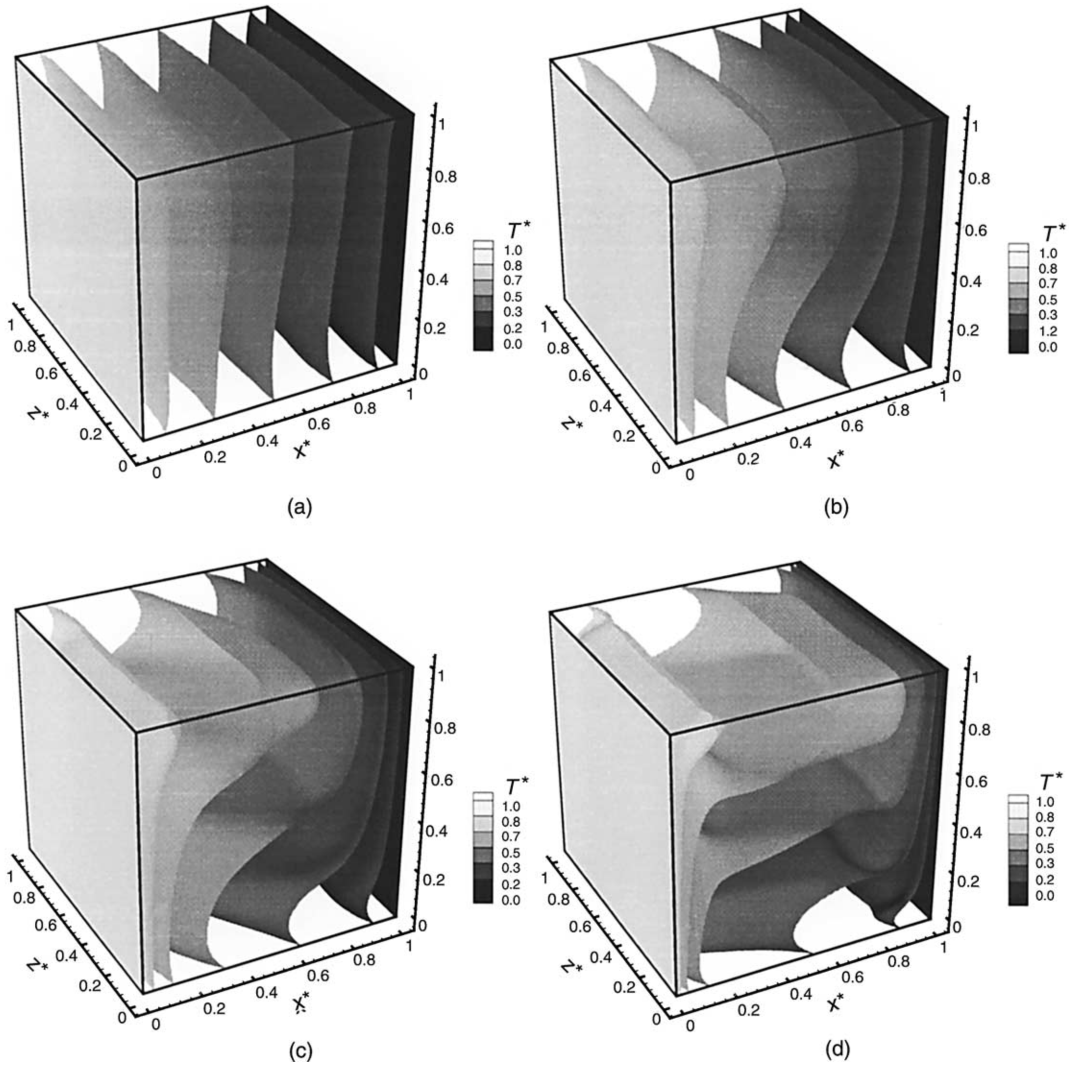

(a) (b) (c) (d)

Fig. 8. Transparent medium, $\tau = 0$. Isothermal surfaces for $Pl = 0.043$, $T_0^* = 15$, $Pr = 0.71$ and four Rayleigh numbers: $Ra = 10^3$ (a), $Ra = 10^4$ (b), $Ra = 10^5$ (c) and $Ra = 10^6$ (d).

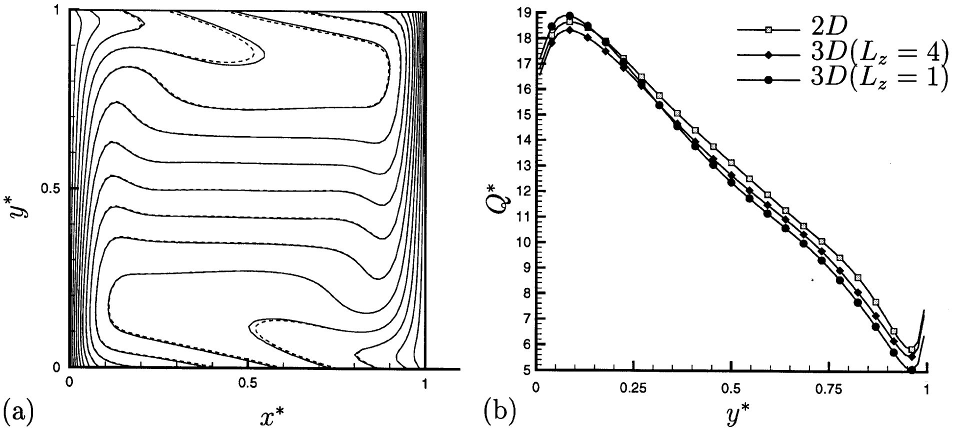

Fig. 9. Comparison between the two-dimensional solution and the three-dimensional stretched cavity. Transparent medium, $\tau = 0$, $Pl = 0.043$, $Pr = 0.71$ and $Ra = 10^6$. Isothermals (solid lines for 3*D* cavity, dashed lines for 2*D* cavity) (a). Local heat flux number at hot wall (b).

In Fig. 8 isothermal surfaces are shown for all Rayleigh numbers considered. For low Rayleigh numbers the conduction heat transfer prevails and the isotherms are nearly vertical (parallel to the gravity field). For high Rayleigh numbers, the isotherms become more horizontal, since the natural convection term, which dominates the conductive term, tends to convey the hottest fluid above the coldest. Thus the isotherms are nearly horizontal (perpendicular to gravity field) in the middle region of the enclosure.

The three-dimensional simulations have been compared to two-dimensional results. The two-dimensional enclosure is discretized in a 65×65 control volume mesh. In Fig. 9(a) the isotherms of the three-dimensional cavity at $z = 2$ (solid lines) and the isotherms of the purely two-dimensional case (dashed lines) are plotted. A good agreement is achieved between both solutions. This means that the effect of the end walls ($z = 0$ and $z = L_z$) is small.

In Fig. 9(b) the local heat flux at the hot wall as a function of the dimensionless height y^* is plotted for the two-dimensional case, for a cubic three-dimensional case and for the mid-plane of the 3D stretched cavity. As the depth L_z of the box increases, the heat flux is closer to the two-dimensional solution. Some differences persist between three-dimensional and two-dimensional cases, probably due to the effects of the end wall.

6.3. Participating medium

Now the medium is assumed to be participating, with a specified optical thickness. The dimensionless reference temperature is fixed to $T_0^* = 17$. In order to emphasize the radiative effects, the Planck number is decreased to $Pl = 0.016$.

In Fig. 10, isothermal surfaces are shown for all Rayleigh numbers tested, and for an optical thickness of $\tau = 10$.

A comparison of the averaged heat flux (in the y^* direction) for three-dimensional situations with participating medium has been carried out. Fig. 11 shows the averaged heat flux versus the depth z^* for several optical thicknesses: $\tau = 0$ (non-participating medium), $\tau = 1$, $\tau = 10$, additive model (optically thick limit) and a non-radiating enclosure.

The participating medium gives lower values of the heat flux than the non-participating one. This decrease is due to the fact that radiative heat flux at the hot wall decreases as the optical thickness increases. The radiative heat exchange takes place between the hot wall and an effective plane which has a higher temperature than the cold wall. It is worth noting that the effect of the increase of the local heat flux at both ends of the z-axis is more important for transparent fluids. As the opacity of the fluid increases, this effect tends to disappear.

In Fig. 12 the detailed contribution of convection and radiation to the total heat flux is shown for different values of Rayleigh number and the optical thickness. The radiation contribution highly depends on the optical thickness τ, while the convection contribution is nearly independent of τ, apart from wall effects on the lower $Ra = 10^3$ case (Fig. 12(a)). Also notice that for the $\tau = 0$ case, the radiation contribution is almost the same for both values of Ra.

The mean heat flux, together with the convection and radiation contribution at the hot wall for different Rayleigh numbers and optical thickness are presented in Table 5. Notice that Q_c^* is nearly independent of the optical thickness, while for $\tau = 0$, Q_r^* remains almost constant for increasing values of the Rayleigh number.

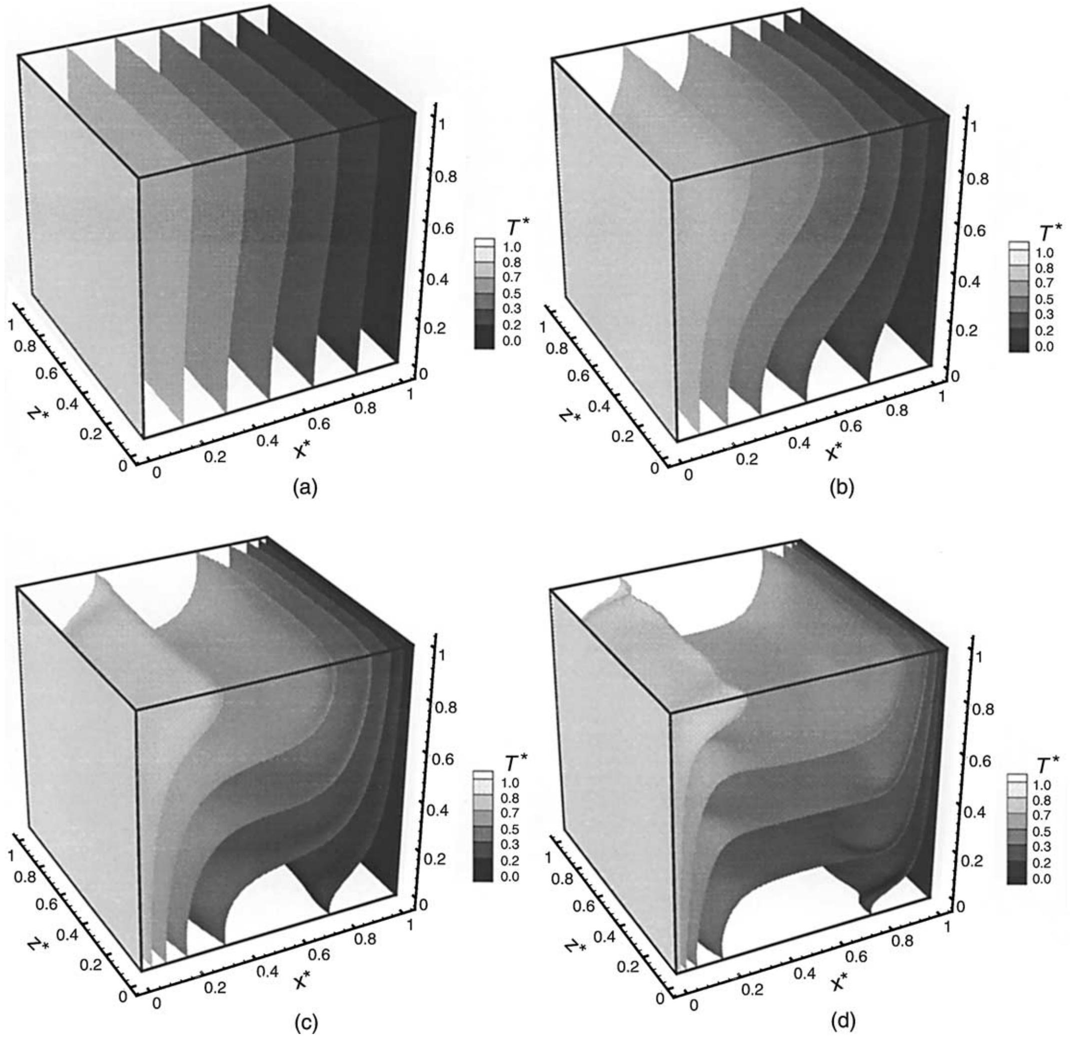

Fig. 10. Participating medium, $\tau = 10$. Isothermal surfaces for $Pl = 0.016$, $T_0^* = 17$ and $Pr = 0.71$ and four Rayleigh numbers: $Ra = 10^3$ (a), $Ra = 10^4$ (b), $Ra = 10^5$ (c) and $Ra = 10^6$ (d).

In Table 6, local values of the velocity field and heat flux are given for a participating medium with $\tau = 10$.

Additional results are presented in Fig. 13. The heat flux increases if the Rayleigh number increases, and it decreases for larger optical thickness. The figure also shows the validity of the additive model for low Rayleigh numbers. Although the additive model is only strictly valid for $\tau \to \infty$, it can be seen in Fig. 13 that it gives reasonable results for low Rayleigh numbers from $\tau \geqslant 30$. For higher values of Ra the optical thickness should be larger in order to apply the additive model.

The problem has also been solved for a range of Planck numbers, for $Ra = 10^6$ and $Ra = 10^5$, $Pr = 0.71$, $T_0^* = 17$ and optical thickness $\tau = 1$. The total heat flux at the hot wall versus the Planck number is plotted in Fig. 14. The two limiting cases are for $Pl \to \infty$, when the conduction heat transfer is more important than the radiative heat transfer (the medium behaves as if no radiation was present), and for $Pl \to 0$ ($k \to 0$), when the medium is at a radiative equilibrium (there is no heat flux due to conduction, and hence $Q^* \to \infty$). The average heat flux behaves as expected and tends to the limiting cases explained above.

7. Conclusions

In this paper, the coupling between radiation and convection has been studied, for both transparent and participating media, in a differentially heated cavity. The influences of Rayleigh and Planck numbers, as well as the optical thickness, are studied.

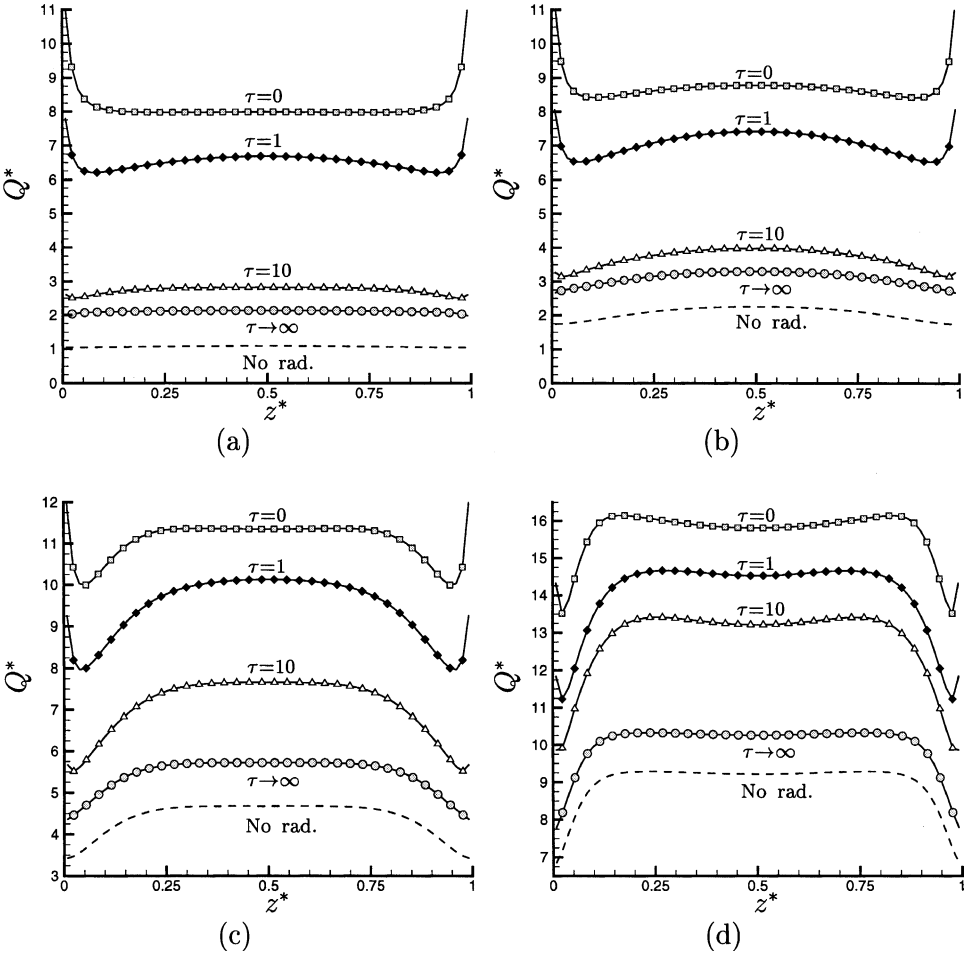

Fig. 11. Average heat flux at hot wall versus depth z^*. Participating medium, $Pl = 0.016$, $T_0^* = 17$ and $Pr = 0.71$ and four Rayleigh numbers: $Ra = 10^3$ (a), $Ra = 10^4$ (b), $Ra = 10^5$ (c) and $Ra = 10^6$ (d).

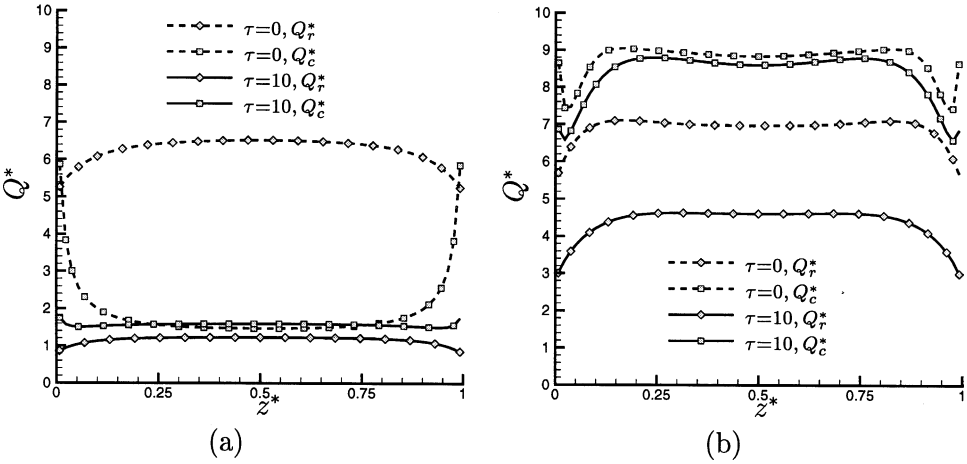

Fig. 12. Plot of detailed convection and radiation contribution to total heat flux through hot wall versus depth z^*. Participating medium, $Pl = 0.016$, $T_0^* = 17$ and $Pr = 0.71$. Two values of Ra are presented: $Ra = 10^3$ (a) and $Ra = 10^6$ (b).

Table 5
Average heat flux at the hot wall for a range of Rayleigh numbers

Ra	$\tau = 30$	$\tau = 10$	$\tau = 1$	$\tau = 0$
10^3	1.80 (0.50,1.30)	2.70 (1.16,1.54)	6.40 (4.64,1.76)	7.96 (6.20,1.76)
10^4	2.87 (0.79,2.08)	3.65 (1.54,2.11)	6.94 (4.69,2.25)	8.54 (6.28,2.26)
10^5	5.94 (1.60,4.34)	7.01 (2.80,4.21)	9.32 (5.44,3.92)	10.89 (6.52,4.37)
10^6	11.54 (2.86,8.68)	12.64 (4.36,8.28)	13.88 (6.25,7.63)	15.48 (6.84,8.64)

Radiative and convective contributions to total heat transfer are shown in parentheses, i.e. (Q_r^*, Q_c^*). Participating medium, with $Pl = 0.016$, $T_0^* = 17$ and $Pr = 0.71$.

Table 6
Local extreme values for velocity and heat flux

	$Ra = 10^3$	$Ra = 10^4$	$Ra = 10^5$	$Ra = 10^6$
v_x^* max	0.1304	0.2720	0.2620	0.1796
y^*	0.823	0.838	0.869	0.900
z^*	0.500	0.500	$0.269^\dagger$	$0.223^\dagger$
v_y^* max	0.1296	0.2805	0.3275	0.3282
x^*	0.177	0.131	0.085	0.038
z^*	0.500	0.500	$0.131^\dagger$	$0.069^\dagger$
Q^* max	3.115	5.767	11.569	22.260
y^*	0.208	0.162	0.161	0.069
z^*	0.500	0.500	$0.346^\dagger$	$0.238^\dagger$
Q^* min	2.147	1.593	1.864	2.658
y^*	~ 1	~ 1	~ 1	~ 1
z^*	$\sim 1^\dagger$	$\sim 1^\dagger$	$\sim 1^\dagger$	$\sim 1^\dagger$

v_x^* max refers the plane $x^* = 0.5$ and v_y^* max to the plane $y^* = 0.5$. The maximum and minimum heat flux refer to the hot wall ($x^* = 0$). The ~ 1 indicates that the maximum was obtained on the last calculation node. The † symbol indicates that the same value was also obtained at location $1 - z^*$. All variables are symmetric respect to the plane $z^* = 0.5$. Participating medium, $\tau = 10$, $Pl = 0.016$, $T_0^* = 17$ and $Pr = 0.71$.

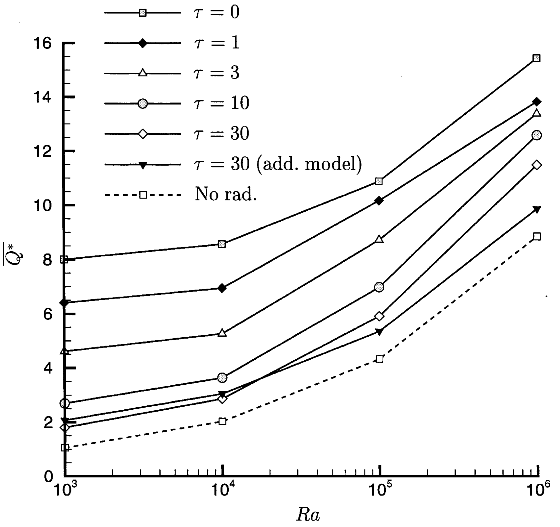

Fig. 13. Mean heat flux at hot wall for several Rayleigh numbers. Participating medium, $Pl = 0.016$, $T_0^* = 17$ and $Pr = 0.71$.

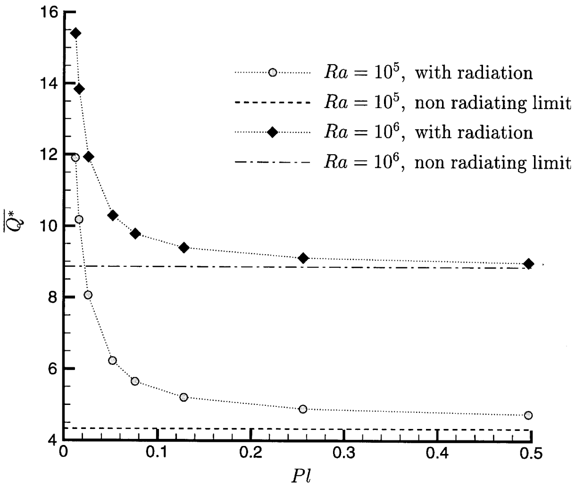

Fig. 14. Total heat flux at hot wall versus Planck number. Participating medium, $\tau = 1$, $T_0^* = 17$, $Pr = 0.71$.

It has been shown that in a transparent medium the radiation significantly increases the heat flux, and that for a given Planck number and constant reference temperature ratio, the contribution of radiation remains almost constant for a range of Rayleigh numbers.

For participating media, defined by its optical thickness, the heat flux also increases as the Rayleigh number increases. On the other hand, an increase on the optical thickness causes a decrease in the heat flux. The optically thick limit tends to the case where radiation is neglected, but with a higher thermal conductivity. The explanation seems to be that, for large optical thickness, radiation becomes a local phenomenon, behaving as a conduction phenomenon, which, according to [13], can be described with the Rosseland radiative conductivity (the so-called diffusion approximation).

Also, for participating media, the additive model has been shown to be accurate for low values of Ra. For higher values of the Rayleigh number, the optical thickness should be larger in order to apply the additive model, which saves computational time and resources.

The effect of the Planck number has also been studied. It has been shown that, for $Pl > 0.5$, the radiation effects can be neglected for low optical thickness. For low Planck numbers ($Pl < 0.01$), the radiation effects dominate and the convection terms of the governing equations can be ignored, and the so-called radiative equilibrium hypothesis can be applied.

All computations presented in this work were performed on a AMD K7 900 Mhz processor with 512 MB of RAM memory. A converged solution of the benchmark problem, with the normalized residual of the temperature field lower than 10^{-9}, takes an average of three days with this computer.

Acknowledgements

This work was supported financially by the "Comsión Interministerial de Ciencia y Tecnología", Spain (project TIC1999-0770), and by the "Comissionat per a Universitats i Recerca de la Generalitat de Catalunya".

References

[1] T. Fusegi, J. Min Hyun, Laminar and transitional natural convection in an enclosure with complex and realistic conditions, Int. J. Heat Fluid Flow 15 (4) (1994) 258–268.
[2] G.D. Vahl Davis, Natural convection of air in a square cavity: a benchmark numerical solution, Int. J. Numer. Meth. Fluids 3 (1983) 249–264.
[3] A. Yücel, S. Acharya, M. Williams, Natural convection and radiation in a square enclosure, Numer. Heat Transfer, Part A 15 (1989) 261–278.
[4] A. Draoui, F. Allard, C. Beghein, Numerical analysis of heat transfer by natural convection and radiation in absorbing, emitting and scattering fluids enclosed in square cavities, Heat Technol. 10 (1–2) (1992) 160–177.
[5] G. Colomer, M. Costa, R. Cònsul, A. Oliva, Radiant exchange in domains with obstacles using the discrete ordinates method, in: 5th ECCOMAS Conference, 2000, pp. 794–803.
[6] N. Selçuk, N. Kayakol, Evaluation of discrete ordinates method for radiative transfer in rectangular furnaces, Int. J. Heat Mass Transfer 40 (2) (1997) 213–222.
[7] M. Mengüç, R. Viskanta, Radiative transfer in three-dimensional rectangular enclosures containing inhomogeneous, anisotropically scattering media, J. Quant. Spectrosc. Radiat. Transfer 33 (6) (1985) 533–549.
[8] J. Truelove, Discrete-ordinate solutions of the radiation transport equations, ASME J. Heat Transfer 109 (4) (1987) 1048–1051.
[9] W. Fiveland, Discrete-ordinates solutions of the radiative transport equation for rectangular enclosures, J. Heat Transfer 106 (1984) 699–706.
[10] M. Modest, Radiative Heat Transfer, McGraw Hill, 1993.
[11] A. Sanchez, T. Smith, Surface radiation exchange for two-dimensional rectangular enclosures using the discrete ordinates method, J. Heat Transfer 114 (1992) 465–472.
[12] A. Ratzell III, J. Howell, J. Heat Transfer 105 (1983) 333.
[13] K. Lee, R. Viskanta, Two-dimensional combined conduction and radiation heat transfer: comparison of the discrete ordinates method and the diffusion approximation methods, Numer. Heat Transfer, Part A 39 (3) (2001) 205–225.